

# Temperature gradients in XMM-Newton observed REFLEX-DXL galaxy clusters at $z \sim 0.3$ \*

Y.-Y. Zhang<sup>1</sup>, A. Finoguenov<sup>1</sup>, H. Böhringer<sup>1</sup>, Y. Ikebe<sup>1,2</sup>, K. Matsushita<sup>1</sup>, and P. Schuecker<sup>1</sup>

<sup>1</sup> Max-Planck-Institut für extraterrestrische Physik, Giessenbachstraße, 85748 Garching, Germany

<sup>2</sup> Joint Center for Astrophysics, University of Maryland, Baltimore County, 1000 Hilltop Circle, Baltimore, MD 21250, USA

Received 5 June 2003 / accepted ...

**Abstract.** We present XMM-Newton results on the temperature profiles of a volume-limited sample of galaxy clusters at redshifts  $z \sim 0.3$ , selected from the REFLEX survey (REFLEX-DXL sample). In the spectral analysis, where only the energies above 1 keV were considered, we obtained consistent results on the temperature derived from the EPN, EMOS1 and EMOS2 data. Useful temperature measurements could be performed out to radii with overdensity 500 ( $r_{500}$ ) for all nine clusters. We discovered a diversity in the temperature gradients at the outer cluster radii with examples of both flat and strongly decreasing profiles. Using the total mass and the gas mass profiles for the cluster RXCJ0307.0–2840 we demonstrate that the errors on the mass estimates for the REFLEX-DXL clusters are within 25% up to  $r_{500}$ .

**Key words.** cosmology: observations – galaxies: clusters: general – X-rays: galaxies: clusters

## 1. Introduction

The volume abundance of galaxy clusters probes the cosmic evolution of large-scale structure (LSS) and thus provides an effective test of cosmological models. It is sensitive to the matter density ( $\Omega_m$ ) and the amplitude of the cosmic power spectra on cluster scale ( $\sigma_8$ ) (e.g. Schuecker et al. 2003). Its evolution is sensitive to the dark energy ( $\Omega_\Lambda$ ) (e.g. Vikhlinin et al. 2002). The most massive clusters are especially important in tracing LSS evolution since they are expected to show the largest evolutionary effects. In addition, the X-ray properties of the most massive clusters should be easier to describe in hierarchical modeling since the structure of the X-ray emitting intracluster plasma is essentially determined by gravitational effects and shock heating. With decreasing cluster mass and intracluster medium (ICM) temperature, non-gravitational effects play an important role before and after the shock heating (Voit & Bryan 2001; Voit et al. 2002; Zhang & Wu 2003; Ponman et al. 2003). Therefore, the most massive clusters provide the cleanest results in comparing theory with observations.

In this project we are analysing a volume-complete sample of thirteen clusters selected from the ROSAT-ESO Flux-Limited X-ray (REFLEX) galaxy cluster survey (Böhringer et al. 2001a) in the redshift interval  $z = 0.27$  to  $0.31$ . With this REFLEX-DXL (Distant X-ray Luminous) sample we like to obtain a robust measure of the cluster abundance of this epoch, in particular to perform studies of the evolution of the cluster population by comparing these observations with more nearby and more distant clusters. A prime goal is to obtain reliable ICM temperatures of these clusters as a measure of the cluster masses (e.g. Evrard 1997). Since peculiarities in the cluster structure introduce a scatter in the mass–temperature relation and since in particular on-going cluster mergers can lead to a temporary increase in the cluster temperature and X-ray luminosity (Randall et al. 2002), we aim for a detailed study of the deep XMM-Newton observations described here. The clusters are also scheduled for a detailed spectroscopic study of the cluster dynamics with the ESO-VLT-VIMOS instrument.

The selection of the REFLEX-DXL sample and its properties are described in detail in Böhringer et al. (2003; Paper I). All clusters selected for this sample have X-ray luminosities in the 0.1–2.4 keV band larger than  $10^{45}$  erg s<sup>−1</sup>. For all clusters in this sample the XMM-Newton observations have confirmed that the X-ray luminosity is dominated by diffuse thermal emission from the ICM of these systems. Therefore, the REFLEX-DXL

---

Send offprint requests to: Y.-Y. Zhang,  
e-mail: yzhang@mpe.mpg.de

\* This work is based on observations made with the XMM-Newton, an ESA science mission with instruments and contributions directly funded by ESA member states and the USA (NASA).

**Table 1.** Compilation of some observational information on the nine REFLEX-DXL clusters. Col. (1): Cluster name. Cols. (2–3): Sky coordinates. Cols. (4–6): Net exposure time of EMOS1, EMOS2 and EPN after cleaning for the flaring episodes. Cols. (7–9): Light curve cleaning criteria. Col. (10): Hydrogen column density in units of  $10^{20}\text{cm}^{-2}$  (Dickey & Lockman 1990). Col. (11): Revolution of XMM-Newton.

Cluster RXCJ	$\alpha$ ( $^{\circ}$ )	$\delta$ ( $^{\circ}$ )	Exposure Time (s)			Criteria Ctr (cts/100s)			$n_{\text{H}}$	XMM orbit
	Eq. J2000.0		EMOS1	EMOS2	EPN	EMOS1	EMOS2	EPN		
0014.3 – 3022	3.583749	–30.375695	15084.5	15510.3	10056.6	23.4	23.7	61.2	1.60	270
0043.4 – 2037	10.850834	–20.622500	11253.2	11247.5	6317.5	23.5	25.0	69.8	1.54	380
0232.2 – 4420	38.071667	–44.345306	11978.7	11507.8	7740.7	22.2	22.4	63.4	2.49	474
0307.0 – 2840	46.766667	–28.670806	12309.4	12610.1	8126.1	21.9	22.5	56.8	1.36	218
0528.9 – 3927	82.234167	–39.463611	7096.9	6805.6	3297.1	23.3	23.2	57.4	2.13	324
0532.9 – 3701	83.235000	–37.026000	10374.2	11190.6	6526.7	23.3	25.3	63.0	2.90	518
0658.5 – 5556	104.570001	–55.960000	25338.7	23365.0	18306.5	24.7	23.6	57.7	6.53	159
1131.9 – 1955	172.985834	–19.925806	11659.5	11164.1	8511.3	22.3	22.3	57.8	4.50	286
2337.6 + 0016	354.420417	0.276000	12216.0	11914.7	7411.8	22.4	23.3	69.1	3.82	365

sample contributes a unique sample of X-ray luminous and consequently very massive clusters from roughly the same epoch, which are not only interesting as cosmological probes, but also for astrophysical studies like the statistics of cluster substructure, galaxy evolution, Sunyaev-Zel’dovich observations and many other applications (e.g. Böhringer et al. 2001b).

The estimate or derivation of the cluster mass is an essential step in almost all these studies. The mass can be either approximately estimated from the temperature (Evrard 1997), or determined from the temperature and density distributions of the ICM under the assumption of hydrostatic equilibrium of the intracluster gas (e.g. Cavaliere & Fusco-Femiano 1976; Serio et al. 1981), or otherwise determined from the mass of the intracluster gas and the assumption of the universality of the cluster baryon fraction (e.g. White et al. 1993; Vikhlinin et al. 2002). The first two methods require a robust determination of the ICM temperature and a good understanding of the cluster structure for a reliable interpretation of the results.

Therefore, it is the aim of this paper to establish a reliable method of spatially resolved temperature determination for the clusters in the REFLEX-DXL sample and to derive temperature profiles for all the clusters. XMM-Newton with its superior sensitivity combined with its good spatial resolution provides the best means for such studies (Arnaud et al. 2002). Previously, large data sets on cluster temperature profiles have been compiled from ASCA (e.g. Markevitch et al. 1998; White 2000; Finoguenov et al. 2001a; Finoguenov et al. 2002; Sanderson et al. 2003) and BeppoSAX observations (Molendi & De Grandi 1999; Ettori et al. 2002).

This paper is structured as follows. In Sect. 2, we describe the background components, which are important to this study. Then we present a double background subtraction method, which is developed to provide a precise background removal. In Sect. 3, we analyse the properties of the hot gas in the galaxy clusters, and show our analytic temperature model. Then we determine the total mass and

gas mass fraction in the cluster RXCJ0307.0–2840 based on the precise temperature and gas density profiles. In Sect. 4, we draw our conclusions. We adopt a flat  $\Lambda$ CDM cosmology with the density parameter  $\Omega_{\text{m}} = 0.3$  and the Hubble constant  $H_0 = 70 \text{ km s}^{-1} \text{ Mpc}^{-1}$ . Errorbars correspond to the 68% confidence level, unless explicitly stated otherwise.

## 2. Method

### 2.1. Data preparation

Of the thirteen XMM-Newton observations of REFLEX-DXL clusters conducted so far, eight have sufficient quality for the detailed studies described here. The remaining five clusters are heavily affected by soft proton flares. Some properties of these observations are described in Paper I. Re-observations of these targets have been proposed and will hopefully be allocated. An additional X-ray luminous REFLEX cluster RXCJ0307.0–2840 at  $z = 0.2532$  was observed in this project and is also analysed here. It has very good observational data and appears to be a very regular and symmetric cluster. We have therefore selected this object as an example to demonstrate our method of analysis.

An overview on the observational data of the complete sample of thirteen plus one clusters is given in Paper I. In this paper we compiled further observational information on the sample targets in Table 1. The observational parameters of the data are described in the following.

We use the XMMSAS v5.4 software for data reduction. The EMOS and EPN data were taken in standard Full Frame mode and Extended Full Frame mode, respectively. For all detectors, the thin filter has been used.

Above 10 keV, there is little X-ray emission from the clusters due to the low telescope efficiency at these energies; the particle background therefore completely dominates. The cluster emission is not variable, so any background can be used for temporal variability studies. Therefore, the energy band 10–15 keV (binned in 100 s in-

**Table 2.** Parameters of the residual background models. Col. (1): Cluster name. Cols. (2–4): Index of the “powerlaw/b” residual background model for EMOS1, EMOS2 and EPN. Cols. (5–7): Normalization of the “powerlaw/b” residual background model for EMOS1, EMOS2 and EPN in unit of  $10^{-4}$  cts  $\text{sec}^{-1}$   $\text{keV}^{-1}$   $\text{arcmin}^{-2}$ .

Cluster	Index			Normalization		
	EMOS1	EMOS2	EPN	EMOS1	EMOS2	EPN
RXCJ0014.3–3022	1.47	1.48	1.95	1.21	1.73	6.49
RXCJ0043.4–2037	1.71	1.43	1.61	1.57	1.28	8.50
RXCJ0232.2–4420	1.26	1.52	1.54	1.26	1.73	6.60
RXCJ0307.0–2840	1.28	1.43	1.82	0.89	1.21	2.80
RXCJ0528.9–3927	0.80	0.96	1.56	0.93	1.12	3.36
RXCJ0532.9–3701	1.60	1.67	2.08	0.32	1.51	3.89
RXCJ0658.5–5556	1.52	1.64	1.95	7.66	3.99	15.26
RXCJ1131.9–1955	1.98	2.34	3.19	1.73	1.89	5.96
RXCJ2337.6+0016	1.24	1.47	1.43	1.71	1.58	8.74

tervals) was used to monitor the particle background and to excise periods of high particle flux. In this screening process we use the settings  $FLAG = 0$  and  $PATTERN < 5$  for EPN, and  $PATTERN < 13$  for EMOS. As an example, Fig. 1 shows the 10–15 keV EPN light curve of RXCJ0658.5–5556.

We reject those time intervals in which the detector countrate (ctr) exceeds a threshold of  $2\sigma$  above the mode countrate of the ctr histogram where  $\sigma$  is determined iteratively by the ctr distribution *below* the mode value where the  $\sigma$  estimates are not affected by flares. A similar cleaning criterion is applied to the screening of the background observation. We note, however, that the thresholds will be different for the source and background accumulations. Formal freezing of the cleaning criteria does not overcome the difference in the mean background countrate. In our analysis we searched through a number of background observations to find the one matching our target observations. The selection criterion is therefore to find the one with a similar cleaning threshold.

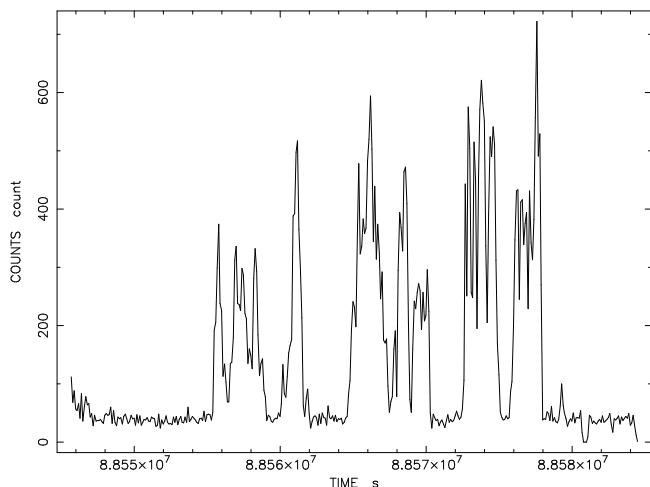


**Fig. 1.** EPN light curve of RXCJ0658.5–5556.

As shown in Table 1, the EPN detector has a similar cleaning threshold for all observations, while the EMOS detectors have higher thresholds for two observations compared to the others. In Sect. 2.2 we consider in detail how this background behaviour affects the temperature determination.

In the analysis of the EPN data, we statistically remove the out-of-time effect using the XMMSAS products.

## 2.2. Background analysis

The purpose of this background analysis described in the following is to find a suitable “blank field” observation to be used for the background subtraction and to further analyse the difference between the target and background to take this residual background into account.

The background has several components which exhibit different spectral and temporal characteristics. In the low energy band ( $< 0.3$  keV), the instrumental background is dominated by electronic noise consisting of a large number of small amplitude events added up during each frame accumulation (Read 2002). This noise depends on the read-out frequency of the cameras and is sensitive to the energy offset of each individual pixel. Energetic particles produce several line and continuum components in the background, which can be further subdivided into time variable and constant components. The constant component has been intensively studied by Lumb et al. (2002) and Read & Ponman (2003). This component can be removed using the so called blank field observations. De Luca & Molendi (2001) report some evidence for a secular evolution of the background level on a half year time scale. Therefore, background accumulations close to the date of the target observation are more suitable. In addition, variations in the instrumental background on a much shorter time scale have been seen (e.g. De Luca & Molendi 2001). Part of such periods with an increased background are rejected through the analysis of the light curve (e.g. Read & Ponman 2003). However, we sometimes still observe a residual enhancement of the background associated with an increase in the quiet flux of soft protons. The

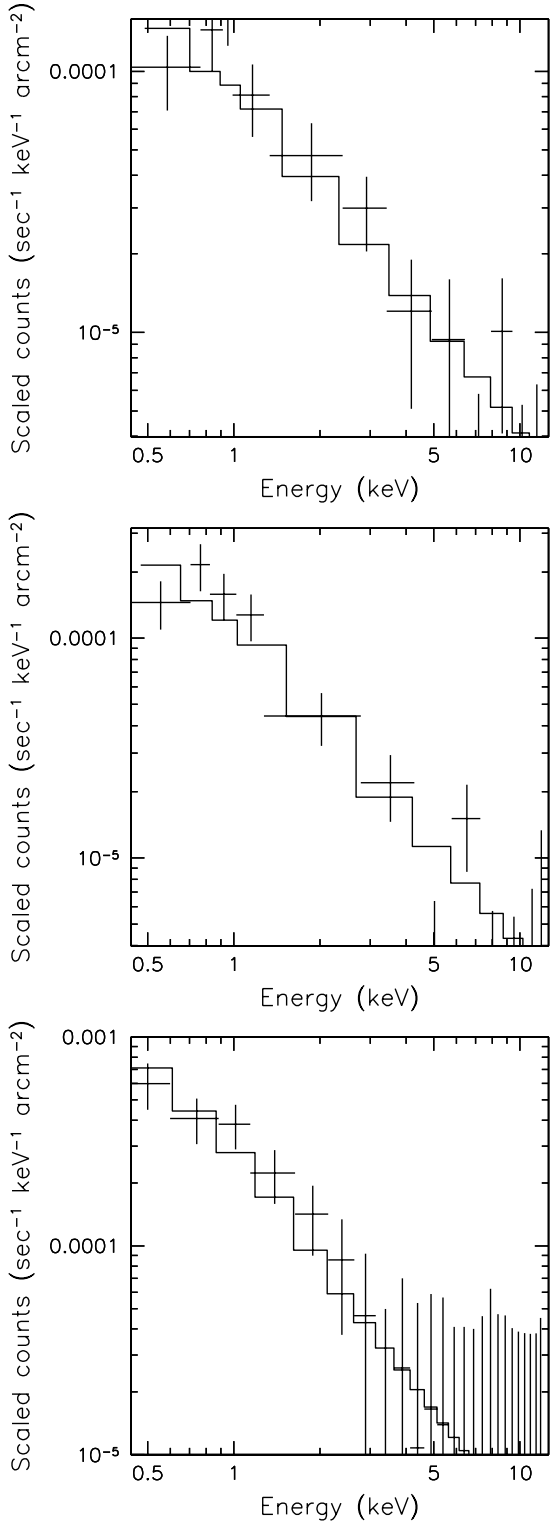


**Fig. 2.** “Powerlaw/b” fits (histogram) of the residual background (solid lines) of RXCJ0307.0–2840 for the region 9.2–11.5′ from the pointing centers of the EMOS1 (top), EMOS2 (middle) and EPN (bottom).

typical time-scale for the variation of this ‘quiet’ component is comparable to or exceeds the typical observational time-scale. Therefore, it is in general not possible to re-

move observational intervals affected by this enhancement. Chen et al. (2003) describe an example of such an observation where quite different ‘quiet’ background levels are observed before and after a flare, respectively.

The photon background consists of foreground emission from the Galaxy as well as the Cosmic X-ray Background (CXB). Observations of the blank field also contain both components, provided the accumulations are done with the same instrumental set-up (e.g. with a particular filter) and the spectra of the X-ray background are the same for both the target and the blank field. This is only guaranteed for the CXB and the emission from the Galaxy halo. Since the Galaxy also plays a role as absorber and foreground emitter, it is important to have a similar absorbing column density for both the target and background accumulations. Additionally, there are some extra galactic components, that display variations. To constrain them, one has to look into the ROSAT All-Sky Survey data around both the background accumulations and the target. Observations with normal conditions of the galactic emission are referred to the quiet galactic zones. So are most of the X-ray background accumulations (Lumb et al. 2002; Read & Ponman 2003). Some source removal is performed on the existing background accumulations. This changes the shape and intensity of the residual CXB. Therefore, a similar source removal has to be performed in the analysis of the target.

Several available XMM-Newton pointings have been investigated. We conclude that the XMM-Newton pointings in the Hubble Deep Field South (HDFS) have similar background conditions as most targets and sufficient exposure time. Therefore, the HDFS is a good candidate for the background for our study. However, there is still a small difference between the background of our sources and the HDFS, which we ascribe mostly to the contamination by soft protons.

We have carefully planned this cluster study such that the cluster radii extent up to spherical overdensities of 500, i.e., the ratio of the mean density of the dark halo with respect to the redshift-dependent critical density  $\rho_{\text{crit}}(z)$ . This is the region to which the cluster X-ray emission is expected to be essentially confined, covering about half of the field of view (FOV) of the XMM-Newton telescope. This enables us to extract a source spectrum from the background region of the target field for comparison with a background spectrum from the background field extracted with the same detector coordinates. Our residual background modeling procedure consists of analysing such regions not affected by cluster emission. We assume little or no vignetting of the soft proton induced background, as suggested by recent studies (Lumb et al. 2002). Spectra are extracted from the region 9.2–11.5′ from the pointing center for our source observations and background candidate observations. In a first step, we compare the spectra extracted from the outer regions in the 0.4–15 keV band between the sources and the background pointings. The residual background signal found from the subtraction of the background field from the target field in this outer

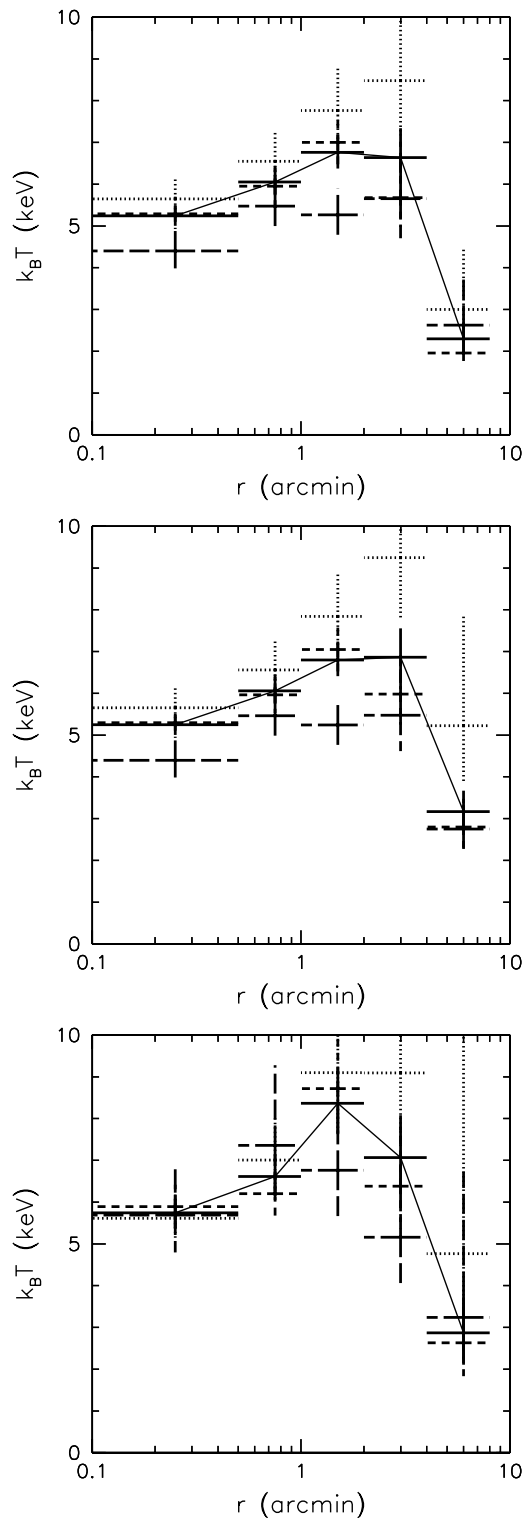


**Fig. 3.** Temperature profiles for RXCJ0307.0–2840 with residual background subtraction (upper panel) and without a residual background subtraction (middle panel) fitted in the 0.4–10 keV band for EMOS1 data (dotted lines), EMOS2 data (dashed lines), EPN data (dash-dotted lines) and combined data (solid lines). The lower panel shows the case with residual background subtraction but fitted in the 1–10 keV band. Additional solid lines connect the temperature measurements for the combined data.

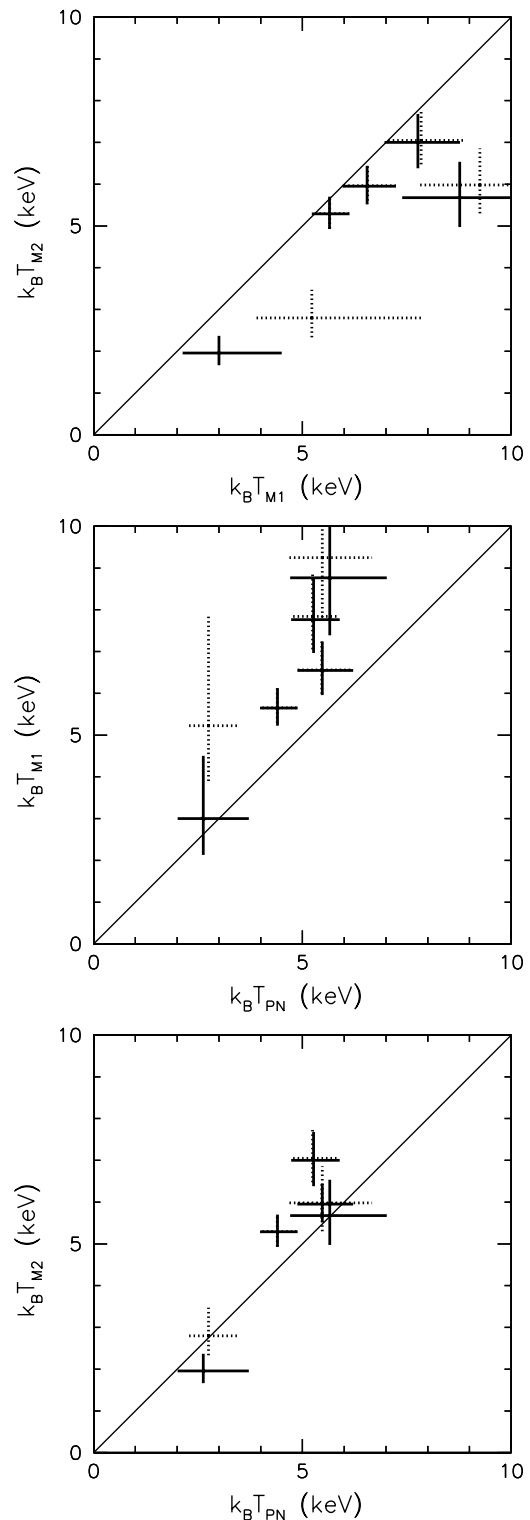


**Fig. 4.** Comparison of the temperature estimates for RXCJ0307.0–2840 from EMOS1, EMOS2 and EPN fitted in the 0.4–10 keV band with (solid lines) and without (dotted lines) a residual background subtraction.

area is then modeled by a “powerlaw/b” spectrum (model name in XSPEC terminology). We use this model to account for the excess soft proton background in our observations as compared to the background field. This residual “powerlaw/b” background model is introduced over the whole energy range by “was\*mekal+powerlaw/b”, which yields after the combination with the blank field background the correct shape of the background component (double background subtraction method). During this procedure, the normalization of the residual background component is always scaled to the area of the source extraction region.

In Fig. 2 we present examples of the residual background. The parameters of the residual background models for the clusters are given in Table 2. The residual background in EPN is higher than in EMOS because the larger thickness of EPN-pixels leads to a higher sensitivity to the particle flux.

To recover the correct spectral shape and normalization of the cluster component, we need both the response matrix file (rmf) and auxiliary response file (arf). We choose the rmf which is normalized to the quantum efficiency. The EPN rmfs that correspond to this choice have a ‘closed’ keyword in their naming conventions. For the EMOS detectors we use a software to generate such files, kindly provided by S. Sembay. The arf contains a table giving the values of areas for a number of different energy ranges. It describes the telescope effective area as a function of photon energy and geometric factors such as bad pixel corrections and detector gaps etc. (around 4 %). It is created by the XMMSAS based command ‘clarf’ provided by A. Finoguenov.

In summary the spectral analysis is performed in two steps. (i) A model for the residual background (background difference) is obtained in XSPEC from a comparison of the outer region of the target and background fields. (ii) The spectral modeling is performed in XSPEC with the cluster region as source data, the HDFS as background and the residual background as a second model component with model parameters fixed to the values found in step (i).

In Fig. 3 we present the temperature profiles resulting from this background subtraction method fitted in the 0.4–10 keV and 1–10 keV bands, respectively, for the example object RXCJ0307.0–2840. We actually compare the results of the two step residual background subtraction with the simple one step background subtraction. One notes that the residual background subtraction provides results in which all three instruments tend to show a better consistency. In Fig. 4 we provide a comparison of the results from EMOS1, EMOS2 and EPN fitted in the 0.4–10 keV band. A detailed treatment of the background does not completely remove the differences between the instruments. We found systematically lower temperatures obtained with EPN compared to EMOS1 and EMOS2 (partially). Since the temperature estimates of EPN are more strongly dependent on the soft energy band compared to EMOS, we have carried out a spectral analysis in the 1–

10 keV band with the results shown in Fig. 3. Despite the larger errorbars, all temperature determinations in the central three bins of the cluster become higher, once the 0.4–1 keV band is excluded. In the following we will systematically investigate the effect of an energy band selection in the temperature and mass estimate.

### 3. Results

#### 3.1. Redshift, mean temperature and metallicity

In a first step of the data analysis we derive global properties of the galaxy clusters. Since a fraction of the clusters have cooling cores, dense central regions with lower temperature and so-called cooling flows, while the others do not display this phenomenon, we derive global temperatures including and excluding these regions. In addition the signal-to-noise decreases fast in the outer regions of the clusters. Therefore, the global temperature was determined in the region  $r < 8'$  and alternatively in the region  $0.5 < r < 4'$ . The global temperatures determined in both regions show some differences. The explanation is partially revealed by the temperature profiles. The metallicities in both zones are very similar.

After subtracting the background and applying the rmf and arf, we fit the spectra in XSPEC using the models of both “mekal\*wabs” and “mekal\*wabs+powerlaw/b”. The fit using the latter model is better. For the radial region  $0.5 < r < 4'$ , we use the 0.4–10 keV and 1–10 keV energy bands. For the region  $r < 8'$ , we use the 1–10 keV energy band. Furthermore, we exclude the regions of the substructure and/or some very bright point sources for several clusters throughout the procedure (cf. Table 3). The temperature of the small and large substructures in the well-known post merger cluster RXCJ0658.5–5556 are  $8.3^{+2.1}_{-1.4}$  keV and  $15.0^{+2.3}_{-1.9}$  keV from the double background subtraction method in the 2–12 keV band. We exclude the small substructure to measure the global temperature.

The measurements of the global temperatures are summarized in Table 4. The global temperatures obtained from model fits to the larger spectral range 0.4–10 keV are always lower compared to the temperatures obtained from 1–10 keV. This discrepancy will be discussed below. The results obtained for the full and restricted spatial zones are consistent within  $1-2\sigma$  (formal errors).

#### 3.1.1. Comparison with previous results

Mushotzky & Scharf (1997) have measured for RXCJ0014.3–3022 a temperature of  $12.08^{+1.42}_{-0.88}$  keV ( $2\sigma$  errors) with ASCA data and give an uncertainty boundary of  $\Delta k_B T / (k_B T) \lesssim 0.3$ . Horner (2001) presents the temperature for the same cluster of  $9.61^{+0.64}_{-0.56}$  keV (reduced  $\chi^2 = 1.02$  for 1002 d.o.f.), for RXCJ0232.2–4420 of  $7.19^{+0.42}_{-0.38}$  keV (reduced  $\chi^2 = 1.09$  for 824 d.o.f.), for RXCJ0307.0–2840 of  $6.71^{+0.60}_{-0.53}$  keV (reduced  $\chi^2 = 1.03$  for 491 d.o.f.), and for RXCJ1131.9–1955 of  $8.26^{+0.63}_{-0.58}$  keV (reduced  $\chi^2 = 0.94$  for 768 d.o.f.), all with  $2\sigma$  errors based

on ASCA data. Lemonon et al. (1997) measured a temperature for the post-merger cluster RXCJ1131.9–1955 of  $5 \pm 3$  keV ( $\chi^2 = 18$  for 16 d.o.f.) using ROSAT PSPC data. They also found some evidence for a temperature gradient.

For the cluster RXCJ0658.5–5556 the published temperature measurements are less consistent. Tucker et al. (1998) measured a temperature of  $17.4 \pm 2.5$  keV ( $2\sigma$  error,  $\chi^2 = 692$  for 778 spectral bins) with ASCA. Andreani et al. (1999) obtained  $14.5^{+2.0}_{-1.7}$  keV using both ASCA and ROSAT data. Yaqoob (1999) measured  $11 \sim 12$  keV with ASCA data. He found that a temperature of  $\sim 17$  keV can be artificially obtained if the true spectrum has a stronger low-energy cut-off than that for Galactic absorption only.

We notice that the ASCA spectra of RXCJ0658.5–5556 have in the 0.5–1 keV band only a few data points with large errorbars. The differences in the temperature measurements described above come therefore clearly from the inclusion or exclusion of this soft part of the spectrum. Studies of the nearby clusters suggest that putative non-thermal and warm thermal components are important at softer energies, while for rich clusters like Coma, the ICM dominates the X-ray emission up to 25 keV (Fusco-Femiano et al. 1999). Non-thermal emission dominates the emission at energies above 3 keV only in some of the groups of galaxies (Fukazawa et al. 2000). Since the expected temperatures of rich clusters are higher than 4 keV, we consider the temperature determination in the hard energy band as a more robust measure of the dominant gas mass component of a cluster, which traces the total mass. For RXCJ0658.5–5556 we decided to restrict our temperature determinations to the energy range 2–12 keV (see Tables 4 and 6).

Our results on RXCJ0658.5–5556 are consistent with Chandra measurements obtained by Markevitch et al.

**Table 3.** Regions with substructures and point sources excluded from the analysis. Col. (1): Cluster name. Col. (2–3): Center of the circle in sky coordinates for J2000.0. Col. (4): Radii. Col. (5): “Yes” if there is an optical point-like counterpart in a digitized optical survey (e.g. DSS2).

Cluster (RXCJ)	$\alpha$ ( $^\circ$ )	$\delta$ ( $^\circ$ )	r ( $''$ )	opt
0014.3–3022	3.63060	−30.37537	15	Yes
	3.51982	−30.41539	15	Yes
	3.51724	−30.41761	10	Yes
	3.53529	−30.36539	30	
0232.2–4420	38.15661	−44.36339	20	Yes
0528.9–3927	82.24274	−39.46467	15	Yes
	82.30713	−39.48091	15	Yes
	82.14495	−39.38667	15	Yes
	82.14353	−39.37243	10	Yes
	82.11335	−39.37130	10	Yes
0532.9–3701	83.19565	−36.94152	15	
	83.15057	−37.02849	10	
0658.5–5556	104.58842	−55.941341	20	

(2002) yielding a temperature of  $14.8^{+1.7}_{-1.2}$  keV from a fit of a spectrum extracted from the central  $r < 3'$  region. Although the authors show that  $k_B T > 15$  keV in some parts of this cluster, the temperatures have quite large errorbars of 7 keV so that we regard this finding as not very significant.

Additionally, Markevitch et al. (2002) fixed the value of the galactic hydrogen column density to  $n_H = 4.6 \times 10^{20} \text{ cm}^{-2}$  which is significantly lower than  $n_H = 6.5 \times 10^{20} \text{ cm}^{-2}$  obtained from Dickey & Lockman (1999). To check this result with our XMM-Newton data we set all parameters to be free to fit the spectrum extracted from the annulus region  $0.5 < r < 4'$  in the 0.4–12 keV band. In this case a high temperature of  $k_B T = 18.8 \pm 2.1$  keV was obtained while the  $n_H$  went down to an unrealistically small value of  $1.8 \pm 0.5 \times 10^{20} \text{ cm}^{-2}$ , although the remaining parameters were still relatively reasonable. Therefore, we decide to fix  $n_H = 6.5 \times 10^{20} \text{ cm}^{-2}$ , but exclude the soft band (0.4–2 keV). In this case we obtained stable results for the temperature, metallicity, and redshift (see Table 4).

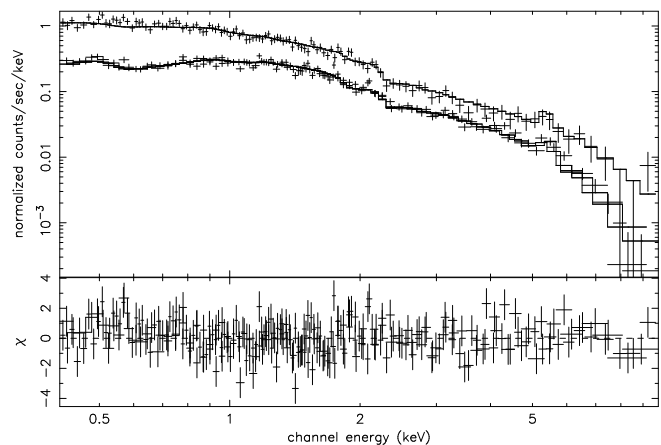


**Fig. 5.** XMM-Newton spectra of RXCJ0307.0–2840 extracted from the region  $0.5 < r < 4'$  obtained with EPN (top) and EMOS (bottom). Model fits: “mekal\*wabs+powerlaw/b” in the 0.4–10 keV band. The residuals are plotted in the lower panel.

The redshifts obtained from the X-ray data (see Table 4) which are ascribed to the ICM, are consistent with the redshifts obtained from optical spectra of individual cluster galaxies (see Böhringer et al. 2003).

We notice that the temperature of RXCJ0528.9–3927 changes most significantly with the lower cut-off of the energy band used in the fit. We thus used the X-ray spectra to test the energy band dependency and possible method dependencies by comparing the results obtained from two different methods and ten different energy bands. For comparison, we use a single-phase temperature with free  $n_H$ , and two double phase models (wabs\*(mekal+mekal)+powerlaw/b and wabs\*(mekal+powerlaw)+powerlaw/b) with fixed  $n_H$  to

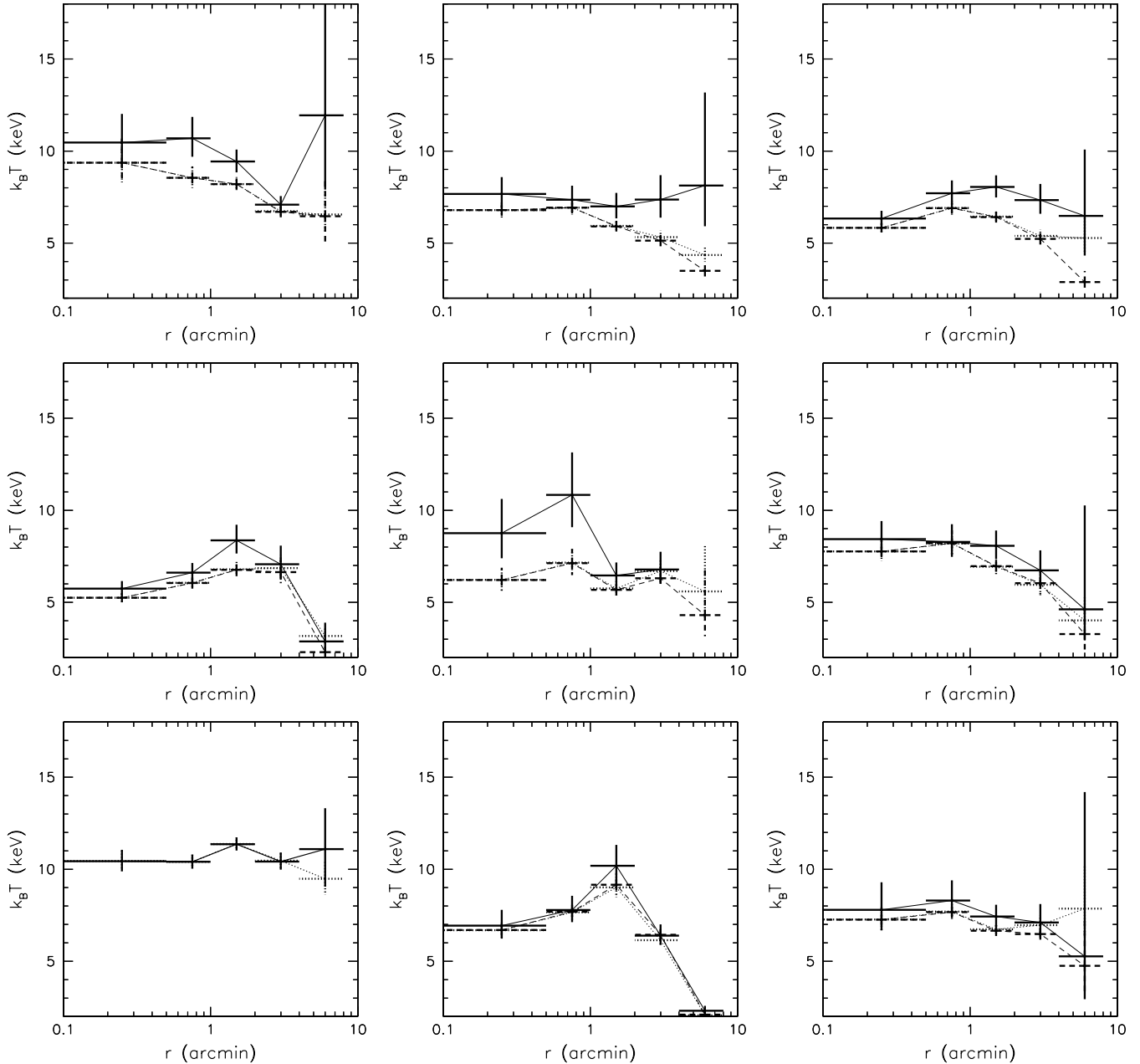


**Fig. 6.** From left to right and from top to bottom, temperature profiles of RXCJ0014.3–3022, RXCJ0043.4–2037, RXCJ0232.2–4420, RXCJ0307.0–2840, RXCJ0528.9–3927, RXCJ0532.9–3701, RXCJ1131.9–1955 and RXCJ2337.6+0016 with (dashed lines) and without (dotted lines) the residual background subtraction fitted in the 0.4–10 keV band. The solid lines present the case with the residual background subtraction but fitted in the 1–10 keV band. The corresponding lines show the temperature profiles. Temperature profiles of RXCJ0658.5–5556 are fitted in 2–12 keV.

fit the spectra in the 0.4–10 keV band. The results presented in Table 5 suggest some influence of the low energy band on the temperature measurements. As we discuss above, the results obtained in the harder energy band should recover the correct cluster temperature. Similar phenomena are also found for A1413 (Pratt & Arnaud 2002) using XMM-Newton data, and Coma, A1795 and A3112 (Nevalainen et al. 2003) based on the comparison of XMM-Newton and ROSAT PSPC observations. Nevalainen et al. interpret this as a soft excess, possibly

due to a ‘warm-hot’ intergalactic medium. We will analyse this feature of our sample in more detail in a forthcoming paper.

### 3.2. Temperature profiles

We have already noted that the differences between the global temperatures of the regions  $0.5 < r < 4'$  and  $r < 8'$  in Table 4 are possibly caused by systematic temperature gradients. For a more detailed study of the temper-

**Table 4.** Global temperatures, metallicities and redshifts of REFLEX-DXL clusters. Col. (1): Cluster name. Col. (2): Radius of annulus in arcminutes. Col. (3): Energy band for fit. Col. (4): X-ray temperature determined in region (2). Col. (5): Metallicity in solar units. Col. (6): Redshift obtained from the X-ray spectrum. Col. (7):  $\chi^2$  per degree of freedom (d.o.f.). Col. (8): Redshift obtained from optical spectra as given in the REFLEX catalogue (see Böhringer et al. 2003). All X-ray spectra are fitted by the XSPEC model “mekal\*wabs+powerlaw/b”.

Cluster	Region	Energy band (keV)	$k_B T$ (keV)	$Z (Z_\odot)$	$z_{X\text{-ray}}$	$\chi^2/d.o.f.$	$z_{opt}$
RXCJ0014.3–3022	$0 < r < 8'$	1–10	$8.65^{+0.43}_{-0.29}$	$0.24^{+0.05}_{-0.04}$	$0.292^{+0.010}_{-0.005}$	392.9/397	0.3080
	$0.5 < r < 4'$	0.4–10	$7.52^{+0.20}_{-0.20}$	$0.22^{+0.03}_{-0.04}$	$0.276^{+0.009}_{-0.009}$	383.2/371	
RXCJ0043.4–2037	$0 < r < 8'$	1–10	$8.30^{+0.43}_{-0.32}$	$0.22^{+0.04}_{-0.05}$	$0.274^{+0.014}_{-0.009}$	269.4/258	
	$0.5 < r < 4'$	0.4–10	$7.50^{+0.47}_{-0.40}$	$0.23^{+0.06}_{-0.06}$	$0.305^{+0.019}_{-0.011}$	198.0/238	0.2924
RXCJ0232.2–4420	$0 < r < 8'$	1–10	$6.01^{+0.23}_{-0.22}$	$0.24^{+0.06}_{-0.06}$	$0.303^{+0.002}_{-0.047}$	195.8/197	
	$0.5 < r < 4'$	0.4–10	$6.89^{+0.43}_{-0.40}$	$0.22^{+0.07}_{-0.07}$	$0.298^{+0.014}_{-0.025}$	123.7/129	
RXCJ0307.0–2840	$0 < r < 8'$	1–10	$6.70^{+0.24}_{-0.25}$	$0.32^{+0.05}_{-0.03}$	$0.276^{+0.002}_{-0.002}$	292.0/332	0.2836
	$0.5 < r < 4'$	0.4–10	$6.33^{+0.22}_{-0.17}$	$0.22^{+0.05}_{-0.03}$	$0.294^{+0.009}_{-0.008}$	384.2/287	
RXCJ0528.9–3927	$0 < r < 8'$	1–10	$7.62^{+0.40}_{-0.33}$	$0.24^{+0.05}_{-0.05}$	$0.296^{+0.009}_{-0.009}$	195.4/195	
	$0.5 < r < 4'$	0.4–10	$6.17^{+0.24}_{-0.27}$	$0.28^{+0.06}_{-0.04}$	$0.241^{+0.003}_{-0.002}$	270.8/281	0.2532
RXCJ0532.9–3701	$0 < r < 8'$	1–10	$6.10^{+0.20}_{-0.22}$	$0.28^{+0.05}_{-0.06}$	$0.243^{+0.004}_{-0.003}$	275.0/251	
	$0.5 < r < 4'$	0.4–10	$6.63^{+0.34}_{-0.31}$	$0.29^{+0.07}_{-0.06}$	$0.241^{+0.006}_{-0.002}$	176.5/167	
RXCJ0658.5–5556	$0 < r < 8'$	1–10	$8.07^{+0.59}_{-0.52}$	$0.31^{+0.08}_{-0.08}$	$0.263^{+0.011}_{-0.013}$	163.2/159	0.2839
	$0.5 < r < 4'$	0.4–10	$6.49^{+0.29}_{-0.27}$	$0.30^{+0.08}_{-0.08}$	$0.281^{+0.011}_{-0.011}$	162.8/148	
RXCJ1131.9–1955	$0 < r < 8'$	1–10	$7.66^{+0.53}_{-0.52}$	$0.28^{+0.10}_{-0.10}$	$0.282^{+0.016}_{-0.016}$	91.5/97	
	$0.5 < r < 4'$	0.4–10	$7.46^{+0.38}_{-0.36}$	$0.34^{+0.07}_{-0.06}$	$0.275^{+0.002}_{-0.004}$	286.1/239	0.2747
RXCJ2337.6+0016	$0 < r < 8'$	1–10	$7.09^{+0.31}_{-0.44}$	$0.29^{+0.08}_{-0.06}$	$0.264^{+0.007}_{-0.012}$	226.5/202	
	$0.5 < r < 4'$	0.4–10	$7.76^{+0.72}_{-0.48}$	$0.28^{+0.10}_{-0.08}$	$0.263^{+0.011}_{-0.021}$	143.7/137	
RXCJ0658.5–5556	$0 < r < 8'$	2–12	$13.59^{+0.71}_{-0.58}$	$0.24^{+0.03}_{-0.03}$	$0.287^{+0.002}_{-0.002}$	621.3/608	0.2994
	$0.5 < r < 4'$	2–12	$14.57^{+0.91}_{-0.69}$	$0.21^{+0.04}_{-0.03}$	$0.291^{+0.004}_{-0.005}$	378.1/400	
RXCJ0658.5–5556	$0 < r < 8'$	1–10	$6.42^{+0.26}_{-0.25}$	$0.26^{+0.05}_{-0.04}$	$0.300^{+0.002}_{-0.003}$	322.5/283	0.3058
	$0.5 < r < 4'$	0.4–10	$6.80^{+0.25}_{-0.23}$	$0.23^{+0.05}_{-0.05}$	$0.300^{+0.010}_{-0.025}$	265.7/258	
RXCJ2337.6+0016	$0 < r < 8'$	1–10	$7.51^{+0.69}_{-0.16}$	$0.27^{+0.04}_{-0.08}$	$0.288^{+0.024}_{-0.016}$	167.0/177	
	$0.5 < r < 4'$	0.4–10	$8.02^{+0.59}_{-0.57}$	$0.22^{+0.06}_{-0.07}$	$0.330^{+0.007}_{-0.011}$	211.1/255	0.2753
RXCJ2337.6+0016	$0 < r < 8'$	1–10	$6.90^{+0.30}_{-0.25}$	$0.25^{+0.05}_{-0.06}$	$0.316^{+0.010}_{-0.012}$	175.1/234	
	$0.5 < r < 4'$	0.4–10	$7.58^{+0.44}_{-0.37}$	$0.22^{+0.06}_{-0.06}$	$0.318^{+0.011}_{-0.012}$	116.2/161	

ature profiles we divide the cluster regions into the five annuli  $0\text{--}0.5'$ ,  $0.5\text{--}1'$ ,  $1\text{--}2'$ ,  $2\text{--}4'$ , and  $4\text{--}8'$  (cf. Fig. 3). Note that in the spectra extracted from the outermost rings of RXCJ0014.3–3022 and RXCJ0528.9–3927 we ignore a narrow energy band containing the residual background around the 1.49 keV Al line (Freyberg et al. 2002).

Table 6 shows the temperature profile catalogue of the clusters from the spectral analysis fitted by “mekal\*wabs” and “mekal\*wabs+powerlaw/b” models. We use both the  $> 0.4$  keV and  $> 1$  keV energy band except for RXCJ0658.5–5556. We apply the 2–12 keV band for this high temperature cluster. The temperature profiles of the clusters are also shown in Fig. 6.

For most of the objects, the temperature can be measured out to  $r_{500}$ . The overall temperature profile is characterized by a rather moderate decrease towards the center, and a decrease towards the outer regions, yet on different levels, including no decrease at all for some of the clusters. This confirms a suggestion of Finoguenov et al. (2001b) that the differences in the behaviour of the temperature profiles in the outskirts of clusters have a statistical origin, rather than simple reflections of measurement errors.

To test the validity of the results without a geometrical deprojection in our analysis, we apply the model ‘project’ in XSPEC to consider the deprojecton effect for RXCJ0307.0–2840. Similar work has been done by Pizzolato et al. (2003). Figure 7 presents the temperature profiles from the spectral fit by “project\*wabs\*mekal” and “project\*wabs\*mekal+powerlaw/b” models in the  $> 0.4$  keV energy band. The temperature gradient becomes slightly more significant when the geometrical deprojection effect is taken into account. The differences are, however, within the errorbars and can thus be neglected.

Systematic differences in the temperature profiles caused by the inclusion of the 0.4–1 keV energy band in the spectral analysis are not the same among the clusters. Cluster RXCJ1131.9–1955 is not affected at all, RXCJ0014.3–3022, RXCJ0307.0–2840 and RXCJ0528.9–3927 are affected in the center, while RXCJ0043.4–2037 and RXCJ0232.2–4420 are affected in the outskirts. Since the instrumental setup used to observe this sample is the same, it hardly is an instrumental artifact. However, more detailed analyses are needed in order to distinguish between the galactic and extragalactic origin of this component in the outskirts of some of the clusters in our sample (e.g. Finoguenov et al. 2003).

**Table 5.** Comparison of temperature, metallicity, and redshift measurements from two different reduction methods and spectral fits performed in ten different energy bands for the cluster RXCJ0528.9–3927. The meanings of the columns are the same as in Table 4.

Energy band (keV)	Method	$k_B T$ (keV)	$Z$ ( $Z_\odot$ )	$z_{X\text{-ray}}$	$\chi^2/d.o.f.$
0.4–10	Free $n_H^a$	$7.69^{+0.28}_{-0.46}$	$0.26^{+0.11}_{-0.07}$	$0.282^{+0.007}_{-0.016}$	126.7/147
	mekal+powerlaw <sup>b</sup>	$8.06^{+2.43}_{-1.19}$	$0.37^{+0.30}_{-0.15}$	$0.291^{+0.020}_{-0.013}$	112.2/145
	mekal+mekal <sup>c</sup>	$9.35^{+10.11}_{-1.06}$	$0.25^{+0.35}_{-0.12}$	$0.285^{+0.026}_{-0.015}$	116.5/142
	Method 1 <sup>d</sup>	$6.49^{+0.29}_{-0.27}$	$0.30^{+0.08}_{-0.08}$	$0.281^{+0.011}_{-0.011}$	162.8/148
	Method 2 <sup>e</sup>	$6.22^{+0.33}_{-0.26}$	$0.31^{+0.10}_{-0.04}$	$0.273^{+0.017}_{-0.012}$	174.1/128
0.7–10	Method 1	$7.22^{+0.45}_{-0.35}$	$0.32^{+0.09}_{-0.09}$	$0.281^{+0.013}_{-0.013}$	110.4/121
	Method 2	$6.87^{+0.33}_{-0.33}$	$0.34^{+0.09}_{-0.08}$	$0.275^{+0.011}_{-0.011}$	122.5/104
0.8–10	Method 1	$7.42^{+0.47}_{-0.39}$	$0.31^{+0.09}_{-0.09}$	$0.281^{+0.012}_{-0.015}$	103.5/113
	Method 2	$6.99^{+0.41}_{-0.38}$	$0.35^{+0.09}_{-0.09}$	$0.275^{+0.014}_{-0.014}$	116.3/97
0.9–10	Method 1	$7.48^{+0.55}_{-0.47}$	$0.31^{+0.10}_{-0.10}$	$0.281^{+0.013}_{-0.015}$	99.4/105
	Method 2	$7.06^{+0.50}_{-0.43}$	$0.33^{+0.11}_{-0.09}$	$0.271^{+0.018}_{-0.017}$	110.7/89
1.0–10	Method 1	$7.66^{+0.64}_{-0.52}$	$0.28^{+0.10}_{-0.10}$	$0.282^{+0.016}_{-0.016}$	91.5/97
	Method 2	$7.33^{+0.54}_{-0.47}$	$0.30^{+0.11}_{-0.09}$	$0.272^{+0.017}_{-0.019}$	101.1/82
1.1–10	Method 1	$7.81^{+0.69}_{-0.57}$	$0.28^{+0.10}_{-0.10}$	$0.281^{+0.016}_{-0.017}$	82.7/89
	Method 2	$7.75^{+0.66}_{-0.57}$	$0.29^{+0.11}_{-0.10}$	$0.271^{+0.017}_{-0.018}$	85.0/74
1.2–10	Method 1	$8.13^{+0.78}_{-0.59}$	$0.26^{+0.10}_{-0.10}$	$0.282^{+0.019}_{-0.021}$	79.0/82
	Method 2	$7.88^{+0.75}_{-0.64}$	$0.29^{+0.12}_{-0.11}$	$0.270^{+0.016}_{-0.030}$	79.9/67
1.3–10	Method 1	$8.17^{+0.83}_{-0.67}$	$0.26^{+0.11}_{-0.10}$	$0.283^{+0.019}_{-0.019}$	74.0/76
	Method 2	$8.03^{+0.80}_{-0.65}$	$0.29^{+0.12}_{-0.10}$	$0.271^{+0.017}_{-0.009}$	76.2/61
1.4–10	Method 1	$7.48^{+0.76}_{-0.61}$	$0.27^{+0.09}_{-0.10}$	$0.281^{+0.016}_{-0.019}$	59.0/70
	Method 2	$7.55^{+0.80}_{-0.67}$	$0.30^{+0.12}_{-0.05}$	$0.272^{+0.016}_{-0.018}$	60.1/56
1.50–10	Method 1	$7.61^{+0.82}_{-0.65}$	$0.27^{+0.10}_{-0.10}$	$0.281^{+0.016}_{-0.019}$	58.0/64
	Method 2	$7.63^{+0.83}_{-0.71}$	$0.30^{+0.12}_{-0.10}$	$0.271^{+0.014}_{-0.017}$	58.9/51

<sup>a</sup> Use the double background subtraction method, but set  $n_H$  to be free. We obtain  $n_H \sim 0 - 0.1 \times 10^{20} \text{ cm}^{-2}$  from the fit to compare with the Galactic value of  $2.1 \times 10^{20} \text{ cm}^{-2}$ .

<sup>b</sup> Use the double background subtraction method, but fit the spectra by model wabs\*(mekal+powerlaw)+powerlaw/b. The powerlaw index of EMOS1, EMOS2 and EPN are  $1.659^{+0.066}_{-0.035}$ ,  $3.211^{+2.109}_{-1.350}$  and  $1.810^{+0.577}_{-0.067}$ . The powerlaw normalizations of EMOS1, EMOS2 and EPN are  $7.96^{+1.04}_{-1.97} \times 10^{-4}$ ,  $8.13^{+19.24}_{-6.88} \times 10^{-5}$  and  $7.06^{+1.28}_{-1.22} \times 10^{-4}$  counts/s/keV, respectively.

<sup>c</sup> Use the double background subtraction method, but fit the spectra by model wabs\*(mekal+mekal)+powerlaw/b. The temperature, metallicity and redshift of the soft component are  $k_B T \sim 0.54\text{--}2.97 \text{ keV}$ ,  $Z_\odot \sim 0.00\text{--}0.06$  and  $z_{X\text{-ray}} \sim 0.000\text{--}2.108$ .

<sup>d</sup> Use the double background subtraction method we have applied throughout this paper.

<sup>e</sup> Use the standard XMMSAS command ‘evigweight’ to correct vignetting, use ‘arfgen’ and ‘rmfgen’ to create on-axis arf and rmf, and apply the blank sky provided by Lumb (2002) to subtract the background (cf. Arnaud et al. 2002).

### 3.3. Modeling RXCJ0307.0–2840

We use RXCJ0307.0–2840 as an illustrative example to demonstrate the accuracy of measurements of the total gravitating cluster mass and the gas mass fraction attainable with the XMM-Newton observations of the REFLEX-DXL-like clusters. Similar analyses of the REFLEX-DXL clusters are in progress. RXCJ0307.0–2840 is also very bright, but at a slightly lower redshift than the selection range for the REFLEX-DXL clusters.

#### 3.3.1. Gas distribution

The regularity of the photon distribution shown in Fig. 8 suggests that there are no large substructures in RXCJ0307.0–2840. We thus assume a radially symmetric gas distribution. In order to get the actual gas distribution we directly deproject the data from the spectroscopic

analysis to get the gas mass profile (cf. Fabian et al 1981; Kriss et al. 1983). We divide the rings used for the temperature determinations into small subrings and fit the normalization for each subring separately, fixing the temperature profile to the values obtained from the above spectral analysis, the metallicities to  $Z = 0.2Z_\odot$ , the redshifts to  $z_{\text{opt}}$  as given in Table 4, and the Galactic absorptions to  $n_H$  as given in Table 1. In the soft band, the X-ray emission is almost independent on the temperature (Fabricant et al. 1980). The gas mass in each spherical shell is proportional to the square root of the integral emission, which can be calculated from the normalization of the spectroscopic analysis (e.g. Vikhlinin et al. 1999).

**Table 6.** Temperature profiles of REFLEX-DXL clusters obtained from spectral analysis with residual background subtraction (double background subtraction) and without residual background subtraction. Col.(1): Cluster name. Col.(2): Energy band for spectral fit. Col.(3): Model used in XSPEC. Cols.(4-8): Temperature measurements. We do not obtain a consistent temperature measurement for RXCJ0528.9–3927 in region 4–8' from the combined data because of the high background.

Cluster	Energy band (keV)	Model	$k_B T$ (keV)				
			$0 < r < 0.5'$	$0.5 < r < 1'$	$1 < r < 2'$	$2 < r < 4'$	$4 < r < 8'$
RXCJ0014.3–3022	0.4-10	model1 <sup>a</sup>	$9.37^{+1.30}_{-1.07}$	$8.54^{+0.62}_{-0.54}$	$8.20^{+0.38}_{-0.35}$	$6.74^{+0.32}_{-0.29}$	$6.56^{+1.30}_{-1.02}$
		model2 <sup>b</sup>	$9.37^{+1.31}_{-1.07}$	$8.55^{+0.62}_{-0.55}$	$8.20^{+0.39}_{-0.35}$	$6.70^{+0.32}_{-0.30}$	$6.46^{+2.14}_{-1.49}$
RXCJ0043.4–2037	0.4-10	model2	$10.46^{+1.56}_{-1.33}$	$10.69^{+1.17}_{-1.00}$	$9.43^{+0.65}_{-0.59}$	$7.09^{+0.47}_{-0.43}$	$11.94^{+11.69}_{-4.03}$
		model1	$6.79^{+0.47}_{-0.41}$	$6.93^{+0.42}_{-0.37}$	$5.93^{+0.31}_{-0.28}$	$5.33^{+0.36}_{-0.34}$	$4.35^{+0.43}_{-0.37}$
RXCJ0232.2–4420	0.4-10	model2	$6.79^{+0.47}_{-0.42}$	$6.93^{+0.42}_{-0.37}$	$5.91^{+0.31}_{-0.28}$	$5.13^{+0.38}_{-0.34}$	$3.49^{+0.46}_{-0.35}$
		model1	$7.67^{+0.92}_{-0.76}$	$7.36^{+0.76}_{-0.66}$	$6.99^{+0.74}_{-0.65}$	$7.37^{+1.32}_{-0.99}$	$8.13^{+5.05}_{-2.21}$
RXCJ0307.0–2840	0.4-10	model1	$5.83^{+0.27}_{-0.25}$	$6.91^{+0.42}_{-0.37}$	$6.44^{+0.32}_{-0.29}$	$5.39^{+0.35}_{-0.34}$	$5.28^{+1.19}_{-0.61}$
		model2	$5.83^{+0.27}_{-0.25}$	$6.90^{+0.42}_{-0.37}$	$6.41^{+0.32}_{-0.30}$	$5.23^{+0.36}_{-0.33}$	$2.88^{+0.61}_{-0.37}$
RXCJ0307.0–2840	1.0-10	model2	$6.34^{+0.42}_{-0.37}$	$7.71^{+0.69}_{-0.60}$	$8.05^{+0.63}_{-0.57}$	$7.34^{+0.87}_{-0.74}$	$6.48^{+3.61}_{-2.16}$
		model1	$5.25^{+0.26}_{-0.24}$	$6.06^{+0.34}_{-0.31}$	$6.80^{+0.42}_{-0.39}$	$6.86^{+0.69}_{-0.61}$	$3.17^{+0.50}_{-0.40}$
RXCJ0528.9–3927	0.4-10	model2	$5.24^{+0.26}_{-0.24}$	$6.05^{+0.34}_{-0.31}$	$6.76^{+0.42}_{-0.39}$	$6.64^{+0.70}_{-0.60}$	$2.30^{+0.40}_{-0.30}$
		model1	$5.74^{+0.40}_{-0.36}$	$6.61^{+0.53}_{-0.46}$	$8.37^{+0.84}_{-0.72}$	$7.07^{+1.01}_{-0.84}$	$2.87^{+1.02}_{-0.63}$
RXCJ0528.9–3927	1.0-10	model2	$6.22^{+0.67}_{-0.58}$	$7.16^{+0.77}_{-0.65}$	$5.75^{+0.43}_{-0.38}$	$6.70^{+0.68}_{-0.58}$	$5.59^{+2.56}_{-1.58}$
		model1	$6.21^{+0.67}_{-0.58}$	$7.12^{+0.76}_{-0.64}$	$5.68^{+0.42}_{-0.37}$	$6.30^{+0.62}_{-0.53}$	$4.30^{+2.67}_{-1.14}$
RXCJ0532.9–3701	0.4-10	model2	$8.75^{+1.86}_{-1.36}$	$10.84^{+2.31}_{-1.76}$	$6.46^{+0.70}_{-0.59}$	$6.79^{+0.96}_{-0.77}$	
		model1	$7.77^{+0.61}_{-0.53}$	$8.19^{+0.70}_{-0.61}$	$6.93^{+0.48}_{-0.43}$	$5.96^{+0.64}_{-0.56}$	$4.02^{+1.24}_{-0.81}$
RXCJ0658.5–5556	2.0-12	model2	$7.77^{+0.61}_{-0.53}$	$8.21^{+0.71}_{-0.61}$	$6.96^{+0.49}_{-0.43}$	$6.04^{+0.69}_{-0.59}$	$3.28^{+1.34}_{-0.89}$
		model1	$8.44^{+0.98}_{-0.81}$	$8.28^{+0.97}_{-0.80}$	$8.07^{+0.83}_{-0.71}$	$6.73^{+1.09}_{-0.85}$	$4.61^{+5.65}_{-1.69}$
RXCJ1131.9–1955	0.4-10	model2	$14.60^{+1.81}_{-1.57}$	$12.94^{+1.13}_{-0.90}$	$14.52^{+0.98}_{-0.91}$	$14.99^{+1.62}_{-1.46}$	$15.72^{+2.40}_{-2.01}$
		model1	$14.57^{+1.57}_{-1.80}$	$12.90^{+1.11}_{-0.89}$	$14.42^{+0.98}_{-0.92}$	$14.33^{+1.68}_{-1.44}$	$11.1^{+2.20}_{-2.00}$
RXCJ2337.6+0016	0.4-10	model2	$6.69^{+0.46}_{-0.41}$	$7.66^{+0.47}_{-0.42}$	$9.02^{+0.61}_{-0.54}$	$6.15^{+0.36}_{-0.33}$	$2.06^{+0.11}_{-0.10}$
		model1	$6.70^{+0.47}_{-0.41}$	$7.69^{+0.47}_{-0.42}$	$9.15^{+0.63}_{-0.56}$	$6.44^{+0.41}_{-0.36}$	$2.10^{+0.14}_{-0.12}$
RXCJ2337.6+0016	1.0-10	model2	$6.93^{+0.86}_{-0.70}$	$7.79^{+0.77}_{-0.66}$	$10.19^{+1.14}_{-0.94}$	$6.39^{+0.61}_{-0.51}$	$2.31^{+0.27}_{-0.22}$
		model1	$7.27^{+0.67}_{-0.58}$	$7.70^{+0.48}_{-0.43}$	$6.73^{+0.31}_{-0.29}$	$6.96^{+0.53}_{-0.46}$	$7.86^{+2.34}_{-1.56}$
RXCJ2337.6+0016	1.0-10	model2	$7.26^{+0.68}_{-0.58}$	$7.67^{+0.48}_{-0.43}$	$6.66^{+0.31}_{-0.29}$	$6.48^{+0.49}_{-0.44}$	$4.75^{+2.52}_{-1.37}$
		model1	$7.80^{+1.49}_{-1.11}$	$8.30^{+1.09}_{-0.86}$	$7.43^{+0.64}_{-0.55}$	$7.11^{+1.00}_{-0.82}$	$5.26^{+8.93}_{-2.33}$

<sup>a</sup> mekal\*wabs.

<sup>b</sup> mekal\*wabs+powerlaw/b.

In Fig. 9 we show the electron number density profiles for RXCJ0307.0–2840. Here, 1 arcmin = 0.237 Mpc at  $z = 0.2532$ . For the fits we use the standard  $\beta$  model

$$n_e(r) = n_{e0} \left[ 1 + \left( \frac{r}{r_c} \right)^2 \right]^{-\frac{3\beta}{2}}, \quad (1)$$

with the core radius  $r_c$  and the shape parameter  $\beta$ . The parameters from the best  $\chi^2$  fits are listed in Table 7. The energy band used for the spectral fits does not affect the normalization, which corresponds to the electron number density profile (cf. Fig. 9).

### 3.3.2. Temperature distribution

The precise estimate of the temperature structure greatly contributes to a reliable mass distribution. The temperature profile of RXCJ0307.0–2840 drops towards the center due to cooling. We found that the parameterization

$$k_B T(r) = \frac{1}{Ar^2 + Br + C} \quad (2)$$

fits the measured temperature profiles quite well. Fig. 10 presents the best  $\chi^2$  fit for RXCJ0307.0–2840 with the parameters given in Table 7. The temperature profile in the outermost regions can be fitted by a polytropic model,  $k_B T(r) = k_B T_0 n_e^{-\gamma}$  (e.g. Finoguenov et al. 2001b). In order to be convectionally stable in the system, the value of  $\gamma$  should not exceed 5/3. Using the results of the spectral analysis in the 0.4–10 keV (1–10 keV) band we obtain  $\gamma = 1.59$  ( $\gamma = 1.46$ ), which fulfills the stability criteria.

### 3.3.3. Mass distribution

We assume the intracluster gas to be in hydrostatic equilibrium with the underlying gravitational potential dominated by the dark matter component. For the cosmological constant  $\Lambda = 0$  we have

$$\frac{1}{\mu m_p n_e} \frac{d(n_e k_B T)}{dr} = -\frac{GM_{DM}(r)}{r^2}, \quad (3)$$

where  $n_e$  and  $k_B T$  are the electron number density and temperature distributions, respectively, and  $\mu = 0.62$

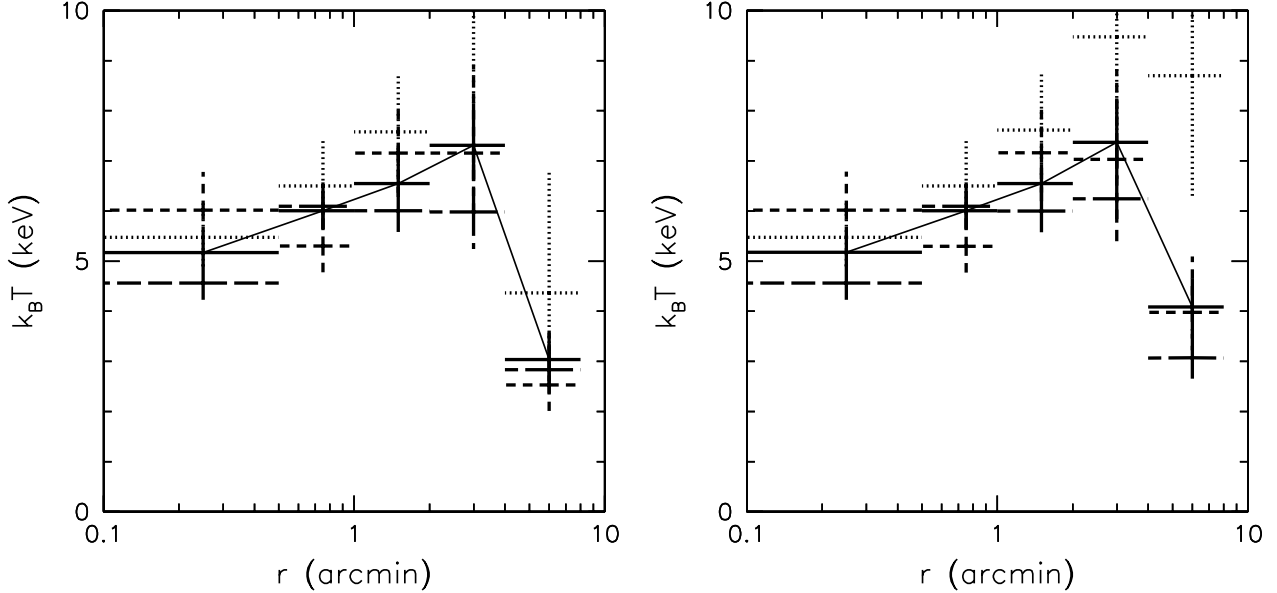


**Fig. 7.** Temperature profiles for RXCJ0307.0–2840 from spectral fits with “projct\*mekal\*wabs+powerlaw/b” (left) and “projct\*mekal\*wabs” (right) models in the 0.4–10 keV energy band for the EMOS1 (dotted lines), EMOS2 (dashed lines), EPN (dash-dotted lines) and combined (solid lines) data. Solid lines connect the temperatures obtained from the combined data.

is the mean molecular weight per hydrogen atom (e.g. Zakamska & Narayan 2003).

Analytic models of the gas density and temperature profiles can be easily combined with Eq.(3) to obtain the mass profile:

$$M(< r) = \frac{r^2}{\mu m_p G} k_B T(r) \left[ \frac{3\beta r}{r_c^2 + r^2} + (2Ar + B)k_B T(r) \right]. \quad (4)$$

We determine the mass distribution by using our temperature model and the  $\beta$  gas density model. We use a Mont-Carlo simulation to calculate the errorbars. We take the approximate expression  $\Delta_c(z) = 18\pi^2 + 82[\Omega_m(z) - 1] - 39[\Omega_m(z) - 1]^2$  as the average overdensity of a dark matter halo within the virial radius  $r_{\text{vir}}$  with respect to the redshift dependent critical density  $\rho_{\text{crit}}(z)$  for a flat universe (Bryan & Norman 1998).

Masses measured by the strong gravitational lensing are sometimes found to be larger compared to the measured masses based on X-rays (Böhlinger et al. 2000; Wu 2000; Wu et al. 1998). High spatially resolved temperature profiles could help to resolve this discrepancy. In order to test the effects of temperature gradients we compare the mass estimates obtained under the assumptions of isothermality using the global temperature as measured in the region  $0.5 < r < 4'$ , and of non-isothermality. The mass and gas mass profiles are plotted in Fig. 11. The virial radius and the total gravitational cluster mass is 2.14 Mpc and  $8.8 \times 10^{14} M_\odot$ , respectively, determined under the assumption of hydrostatic equilibrium and isothermality.

### 3.3.4. Modeling NFW mass distribution

Navarro et al. (1997; NFW) present a universal density profile from numerical simulations in hierarchical clustering scenarios,

$$\rho_{\text{DM}}(r) = \frac{\delta_{\text{crit}} \rho_{\text{crit}}}{(r/r_s)(1 + r/r_s)^2}, \quad (5)$$

where  $\delta_{\text{crit}}$  and  $r_s$  are the characteristic density and scale of the halo, respectively, and  $\rho_{\text{crit}}$ , the critical density of the universe at the cosmic epoch  $z$ .  $\delta_{\text{crit}}$  is related to the concentration parameter of a dark halo  $c = r_{\text{vir}}/r_s$  by

$$\delta_{\text{crit}} = \frac{200}{3} \frac{c^3}{\ln(1+c) - c/(1+c)}. \quad (6)$$

We fit the observational temperature profile to obtain the parameters  $\rho_s = \delta_{\text{crit}} \rho_{\text{crit}}$  and  $r_s$  if we assume that the hot gas is in hydrostatic equilibrium with the dark matter. The former is well fitted by a standard  $\beta$  profile. The parameters of the best fit of the NFW profile are presented in Table 7.

The NFW model well describes the mass and gas mass fraction in the outer region. Due to the cuspy NFW profile in the cluster center, the temperature fit based on the NFW model is higher than the observations. As a result, the gas mass fraction becomes lower in the center.

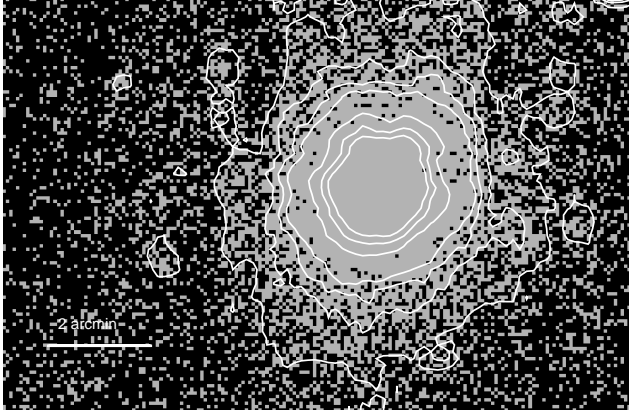


**Fig. 8.** Merged image from the three instruments for RXCJ0307.0–2840 in the 0.5–2 keV band. Superposed contours suggest a quite regular morphology.

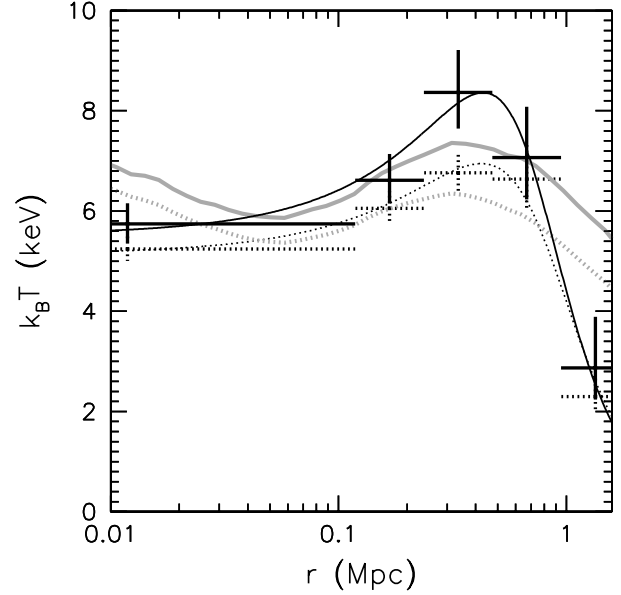


**Fig. 10.** Measured temperatures of RXCJ0307.0–2840 fitted in the 0.4–10 keV band (dotted lines) and 1–10 keV band (solid lines). The corresponding curves show the best fit using the NFW profile (light black) and Eq.(2) (dark black).

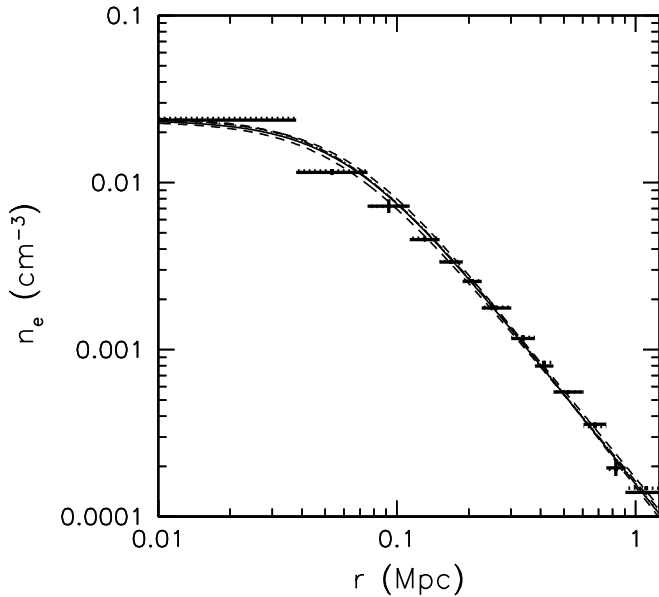


**Fig. 9.** Measured electron number density profiles of RXCJ0307.0–2840 fitted in the 0.4–10 keV (dotted lines) and 1–10 keV (solid lines), respectively. The corresponding curves present the best fit using the standard  $\beta$  model with the confidence intervals (dashed curves).

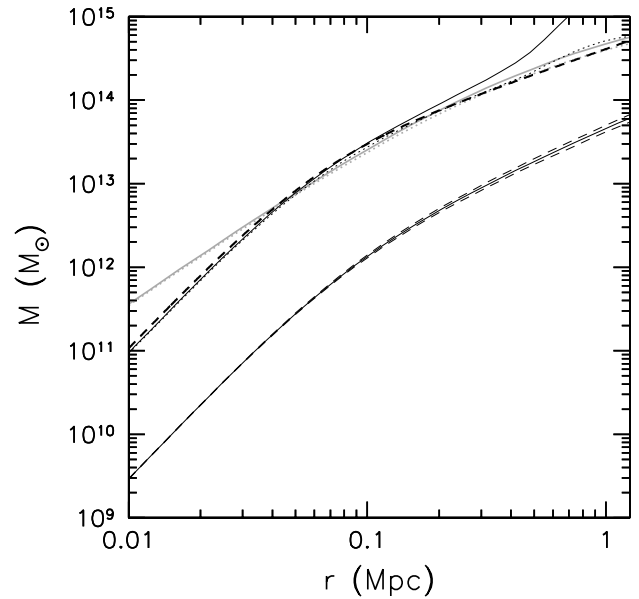


**Fig. 11.** Mass profiles (top) for RXCJ0307.0–2840 based on the temperature measurements fitted in the 0.4–10 keV band (dotted curves) and 1–10 keV band (solid curves) using the NFW model (light black) and Eq.(4) (dark black). An additional dashed curve presents the mass profile under the assumption of isothermality. The solid curve (bottom) with the confidence intervals (dashed curves) presents the gas mass distribution.

### 3.3.5. Modified hydrostatic equilibrium with $\Lambda$

To be consistent with our background cosmological model with  $\Lambda \neq 0$  we should expect a second-order modification of the equation of hydrostatic equilibrium in the form

$$\frac{1}{\mu m_p n_e} \frac{d(n_e k_B T)}{dr} = -\frac{GM_{\text{DM}}(r)}{r^2} + \frac{\Lambda c^2}{3} r. \quad (7)$$

In Fig. 12 we present both the fraction  $\Lambda c^2 r^3 / (3GM_{\text{DM}}(r))$  caused by the  $\Lambda$  term and the relative error  $\Delta M_{\text{DM}}(r) / M_{\text{DM}}(r)$ , where  $M_{\text{DM}}$  and  $\Delta M_{\text{DM}}(r)$  are obtained from Sect. 3.3.3 and Sect. 3.3.4. It is seen that the effect of a non-zero  $\Lambda$  is smaller than one percent and can thus be neglected in our mass estimations. Sussman & Hernandez (2003) also point out a small effect of  $\Lambda$  on virialized structures, and that it could be significant only in the linear regime on large scales of  $r \sim 30$  Mpc.

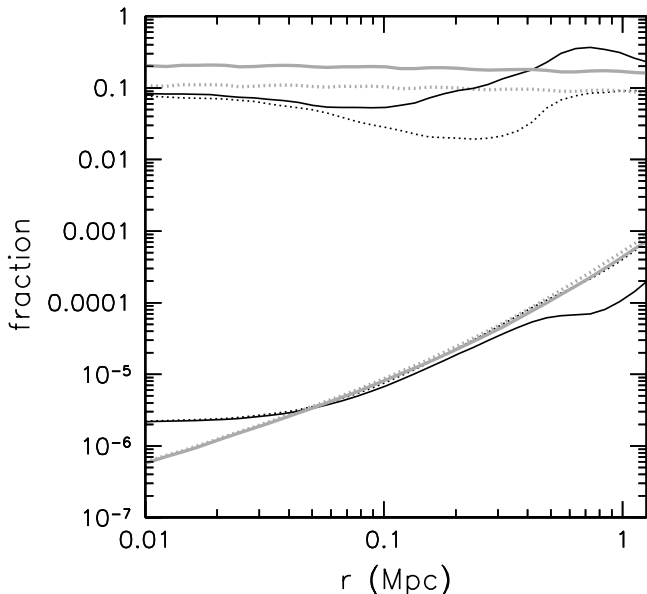


**Fig. 12.** Fraction  $\Lambda c^2 r^3 / (3GM_{\text{DM}}(r))$  (bottom) and the relative error  $\Delta M_{\text{DM}}(r) / M_{\text{DM}}(r)$  (top) based on the temperature measurements fitted in the 0.4–10 keV band (dotted curves) and 1–10 keV band (solid curves) using the NFW model (light black) and Eq.(4) (dark black), where  $M_{\text{DM}}$  and  $\Delta M_{\text{DM}}(r)$  are obtained from Sect. 3.3.3 and Sect. 3.3.4 .

### 3.3.6. Gas mass fraction distribution

The distribution of the gas mass fraction is obtained according to the definition  $f_{\text{gas}}(r) = M_{\text{gas}}(r) / M_{\text{DM}}(r)$ . Since the derived gas mass is not completely unrelated to the derived total mass, we calculate the errorbars of the gas fraction,  $\Delta f_{\text{gas}} = (\Delta M_{\text{gas}} M_{\text{DM}} + M_{\text{gas}} \Delta M_{\text{DM}}) / M_{\text{DM}}^2$ . The profile of the gas mass fraction based on the NFW modeling is steeper in the central region as seen in Fig. 13. In both mass modelings the gas fractions increase with radius, and range from  $f_{\text{gas}} = 0.035 \pm 0.012$  to  $0.138 \pm 0.026$  in the outermost regions ( $r_{\text{out}} = 1.422$  Mpc) (see Table 7).

These results are in good agreement with the measurements of Allen et al. (2002) based on Chandra observations of seven clusters yielding  $f_{\text{gas}} \sim 0.105\text{--}0.138$ , and with the measurements of Sanderson et al. (2003) based on ASCA GIS & SIS and ROSAT/SPSP observations of 66 clusters yielding  $f_{\text{gas}} = 0.13 \pm 0.01 h_{70}^{-3/2}$ . Our value is also very close to the universal baryon fraction obtained with the recent WMAP measurement  $f_b = \Omega_b / \Omega_m = 0.166$ , where  $\Omega_b h^2 = 0.0224$  and  $\Omega_m h^2 = 0.135$  (Spergel et al. 2003). This reassures the estimate of the mass distribution.

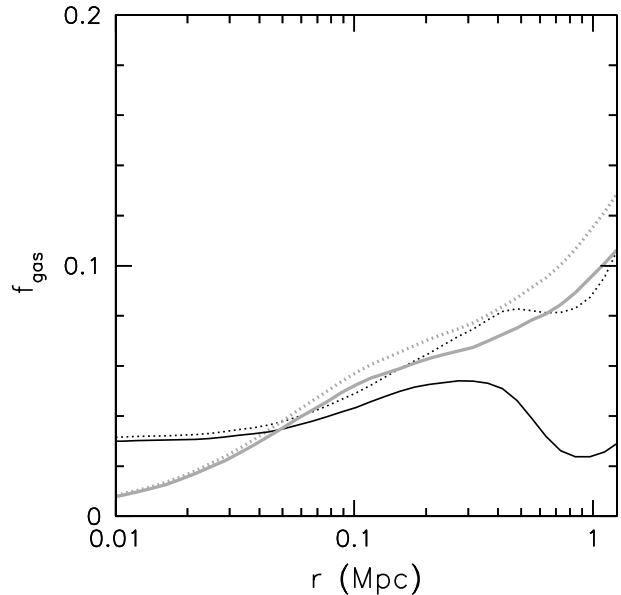


**Fig. 13.** Gas mass fraction distributions based on the temperature measurements fitted in the 0.4–10 keV band (dotted curves) and 1–10 keV band (solid curves) using the NFW model (light black) and Eq.(4) (dark black).

We also make use of the region  $8 < r < 10'$  to obtain an upper limit of the gas mass in this shell applying the model “mekal+wabs” without residual background subtraction. The upper limit of the total gas mass within 10 arcmin (2.37 Mpc) is  $2.49 \times 10^{14} M_{\odot}$ . Based on the above mass modeling described by Eq.(4), the upper limit of the gas fraction within 10 arcmin is 0.49. This unreasonably high value confirms that the background dominates in this region.

## 4. Summary and Conclusions

We studied eight clusters of the REFLEX-DXL sample, selected from the REFLEX clusters at redshifts around  $z \sim 0.3$ , and one supplementary cluster. The data are from the EMOS1, EMOS2 and EPN detectors of XMM-Newton. The consistent results from the three detectors, obtained by excluding the energies below 1 keV, give a good confidence in the applied method and provide tight constraints on the ICM parameters like the temperature, metallicity, and redshift.

Some of the clusters have been previously studied with ASCA, ROSAT and Chandra. The Chandra measurement

**Table 7.** Parameters of each model from the best  $\chi^2$  fits.  $r_{\text{out}} = 1.422$  Mpc is the outermost region where we can measure these parameters.  $r_{500}$  and  $r_{\text{vir}}$  are measured from the data.

Model	parameter	0.4–10 keV	1–10 keV
$\beta$	$r_c$ (Mpc)	$0.061 \pm 0.004$	$0.062 \pm 0.004$
	$n_{e0}$ ( $10^{-2} \text{cm}^{-3}$ )	$2.43 \pm 0.03$	$2.37 \pm 0.04$
	$\beta$	$0.60 \pm 0.02$	$0.60 \pm 0.02$
Eq.(2)	$A$ ( $\text{Mpc}^{-2} \text{keV}^{-1}$ )	$0.283 \pm 0.046$	$0.331 \pm 0.082$
	$B$ ( $\text{Mpc}^{-1} \text{keV}^{-1}$ )	$-0.240 \pm 0.028$	$-0.285 \pm 0.052$
	$C$ ( $\text{keV}^{-1}$ )	$0.195 \pm 0.004$	$0.181 \pm 0.007$
NFW	$r_s$ (Mpc)	$0.267 \pm 0.028$	$0.306 \pm 0.034$
	$\rho_s$ ( $10^{15} \text{M}_\odot \text{Mpc}^{-3}$ )	$2.183 \pm 0.311$	$1.945 \pm 0.504$
	$c$	$5.805 \pm 0.588$	$5.559 \pm 0.681$
	$M_{500}$ ( $10^{14} \text{M}_\odot$ )	$4.103 \pm 0.374$	$5.125 \pm 0.850$
	$r_{500}$ (Mpc)	1.038	1.116
	$M_{\text{vir}}$ ( $10^{14} \text{M}_\odot$ )	$5.524 \pm 0.487$	$7.125 \pm 1.175$
	$r_{\text{vir}}$ (Mpc)	1.550	1.701
	$f_{\text{gas}}(r < r_{\text{vir}})$	$0.144 \pm 0.028$	$0.124 \pm 0.036$
	$M_{r_{\text{out}}}$ ( $10^{14} \text{M}_\odot$ )	$5.168 \pm 0.456$	$6.296 \pm 1.037$
	$f_{\text{gas}}(r < r_{\text{out}})$	$0.138 \pm 0.026$	$0.112 \pm 0.032$
Eq.(4)	$M_{500}$ ( $10^{14} \text{M}_\odot$ )	$6.861 \pm 0.012$	$5.168 \pm 0.849$
	$r_{500}$ (Mpc)	1.231	1.118
	$M_{r_{\text{out}}}$ ( $10^{14} \text{M}_\odot$ )	$6.906 \pm 0.001$	$16.46 \pm 4.69$
	$f_{\text{gas}}(r < r_{\text{out}})$	$0.103 \pm 0.010$	$0.035 \pm 0.012$

of the temperature of RXCJ0658.5–5556 includes mainly the central region  $r < 3'$ , where the temperature is high. We measure the global temperatures over a larger radial range  $0.5 < r < 4'$  and  $r < 8'$ , respectively.

The parameter which best characterizes cluster masses, and which is most relevant for studies of the LSS and cosmology, is the hot temperature of the bulk of the ICM. To avoid contamination by a possible central cooling core and by a possible soft excess or residual calibration uncertainties, we excluded the central region  $r < 0.5'$  and the softest part of the X-ray spectrum ( $< 1$  keV) yielding the reliable temperatures. These are the global temperatures that will be used in Paper I to derive the X-ray temperature function for this sample.

We obtained the spatially resolved X-ray temperature profiles for each cluster. For the determination of temperature profiles, the good statistics of the data allowed us to derive temperature values in five radial bins. In the inner regions an accuracy of better than 10–20 % can still be derived while the errors increase in the outer or outermost two bins. The temperature varies as a function of radius by factors of 1.5–2. The intracluster gas is cool in the center of RXCJ0232.2–4420, RXCJ0307.0–2840, RXCJ0528.9–3927, and RXCJ1131.9–1955. No significant cooling gas is found with temperatures below 2 keV. In the outer region, the temperature drops at different levels. The differences of the temperature profiles in the cluster center may reveal that some clusters have relaxed cooling cores (but not all) and to some degree that we see the effect of non-gravitational processes. In this respect, it is remarkable that cooling cores are not only found in clusters with symmetric and regular X-ray images which

might suggest a relaxed dynamical state, but also in the elongated, very disturbed cluster RXCJ1131.9–1955.

To study RXCJ0307.0–2840 in detail, we find a model which fit the complex temperature profile of this cluster quite well.

The mass distribution of this cluster, based on the precise measurements of the distributions of the temperature and gas density, is similar to the mass distribution obtained under the assumption of isothermality within the region we can measure. We investigated the gas mass fraction of RXCJ0307.0–2840 and find an increasing gas mass fraction as a function of radius, which is typical for most clusters. In the outermost region of the cluster, it approaches the value of the universal baryon fraction. The uncertainty of the gas fraction is mainly caused by the temperature measurement. Therefore, a reliable determination of the temperature profile is a key point to obtain a precise estimate of both the mass and the gas mass fraction. It plays an important role in the M-T scaling relation.

*Acknowledgements.* The XMM-Newton project is supported by the Bundesministerium für Bildung und Forschung, Deutsches Zentrum für Luft und Raumfahrt (BMBF/DLR), the Max-Planck Society and the Haidenhaim-Stiftung. We acknowledge Jacqueline Bergeron, PI of the XMM-Newton observation of the HDFs, and Martin Turner, PI of the XMM-Newton observation of RXJ0658.5–5556. We acknowledge Steve Sembay who kindly provides us the software to generate the rmf for EMOS and Wolfgang Pietsch, Michael Freyberg, Frank Haberl and Ulrich G. Briel providing useful suggestions. YYZ acknowledges receiving the International Max-Planck Research School Fellowship. AF acknowledges receiving the Max-Planck-Gesellschaft Fellowship. PS acknowledges support under the

DLR grant No. 50 OR 9708 35. YYZ thanks Linda Pittroff for careful reading the manuscript and useful suggestions.

## References

- Allen, S. W., Schmidt, R. W., & Fabian, A. C., 2002, *MNRAS*, 334, 11
- Andreani, P., Böhringer, H., dall'Oglio, G., et al., 1999, *ApJ*, 513, 23
- Arnaud, M., Majerowicz, S., Lumb, D., et al., 2002, *A&A*, 390, 27
- Böhringer, H., Soucaill, G., Mellier, Y., Ikebe, Y., & Schuecker, P., 2000, *A&A*, 353, 124
- Böhringer, H., Schuecker, P., Guzzo, L., et al., 2001a, *A&A*, 369, 826
- Böhringer, H., Schuecker, P., Lynam, P., et al., 2001b, *Msngr*, 106, 24
- Böhringer, H., Schuecker, P., Zhang, Y.-Y., et al., 2003, preprint, *A&A*, to be submitted (Paper I)
- Bryan, G. L., & Norman, M. L., 1998, *ApJ*, 495, 80
- Cavaliere, A., & Fusco-Femiano, R., 1976, *A&A*, 49, 137
- Chen, Y., Ikebe, I., & Böhringer, H., 2003, preprint, *A&A*, submitted
- De Luca, A. & Molendi, S., 2001, in Proceedings of the Symposium 'New Visions of the X-ray Universe in the XMM-Newton and Chandra era', ESTEC, Noordwijk, The Netherlands, in press
- Dickey, J. M., & Lockman, F. J., 1990, *ARAA*, 28, 215
- Ettori, S., De Grandi, S., & Molendi, S., 2002, *A&A*, 391, 841
- Evrard, A. E., 1997, *MNRAS*, 292, 289
- Fabian, A. C., Hu, E. M., Cowie, L. L., Grindlay, J., 1981, *ApJ*, 248, 47
- Fabricant, D., Lecar, M., & Gorenstein, P., 1980, *ApJ*, 241, 552
- Finoguenov, A., Arnaud, M., & David, L. P., 2001a, *ApJ*, 555, 191
- Finoguenov, A., Briel, U. G., & Henry, J. P., 2003, preprint, *A&A*, submitted
- Finoguenov, A., Jones, C., Böhringer, H., & Ponman, T. J., 2002, *ApJ*, 578, 74
- Finoguenov, A., Reiprich, T. H., & Böhringer, H., 2001b, *A&A*, 368, 749
- Freyberg, M. J., Pfeffermann, E., & Briel, U. G., 2002, in Symp. New Visions of the X-ray Universe in the XMM-Newton and Chandra Era (ESA SP-488; Noordwijk: ESA), in press
- Fukazawa, Y., Makishima, K., Tamura, T., et al., 2000, *MNRAS*, 313, 21
- Fusco-Femiano, R., dal Fiume, D., Feretti, L., et al. 1999, *ApJ*, 513, 21
- Horner, H., 2001, Ph.D. thesis, X-ray Scaling Laws for Galaxy Clusters and Groups
- Kriss, G. A., Cioffi, D. F., Canizares, C. R., 1983, *ApJ*, 272, 439
- Lemonon, L., Pierre, M., Hunstead, R., et al., 1997, *A&A*, 326, 34
- Lumb, D. H., Warwick, R. S., Page, M., & De Luca, A., 2002, *A&A*, 389, 93
- Markevitch, M., Forman, W. R., Sarazin, C. L., & Vikhlinin, A., 1998, *ApJ*, 503, 77
- Markevitch, M., Gonzalez, A. H., David, L., et al., 2002, *ApJ*, 567, 27
- Molendi, S., & De Grandi, S., 1999, *A&A*, 351, 41
- Mushotzky, R. F. & Scharf, C. A., 1997, *ApJ*, 482, 13
- Navarro, J. F., Frenk, C. S., & White, S. D. M., 1997, *ApJ*, 490, 493 (NFW)
- Nevalainen, J., Lieu, R., Bonamente, M., & Lumb, D., 2003, *ApJ*, 584, 716
- Pizzolato, F., Molendi, S., Ghizzardi, S., & De Grandi, S. 2003, preprint [astro-ph/0304016]
- Ponman, T. J., Sanderson, A. J. R., & Finoguenov, A., 2003, preprint [astro-ph/0304048]
- Pratt, G. W., & Arnaud, M., 2002, *A&A*, 394, 375
- Randall, S. W., Sarazin, C. L., & Ricker, P. M., 2002, *AAS*, 201, 6706
- Read, A. M., 2002, preprint [astro-ph/0212436]
- Read, A. M., & Ponman, T. J., 2003, preprint [astro-ph/0304147]
- Sanderson, A. J. R., Ponman, T. J., Finoguenov, A., Lloyd-Davies, E. J., Markevitch, M., 2003, *MNRAS*, 340, 989
- Schuecker, P., Böhringer, H., Collins, C. A., & Guzzo, L., 2003, *A&A*, 398, 867
- Serio, S., Peres, G., Vaiana, G. S., Golub, L., & Rosner, R., 1981, *ApJ*, 243, 288
- Spergel, D. N., Verde, L., Peiris, H. V., et al., 2003, preprint [astro-ph/0302209]
- Sussman & Hernandez, 2003, preprint [astro-ph/0304385]
- Tucker, W., Blanco, P., Rappoport, et al., 1998, *ApJ*, 496, 5
- Vikhlinin, A., VanSpeybroeck, L., Markevitch, M., Forman, W. R., & Grego, L., 2002, *ApJ*, 578, 107
- Vikhlinin, A., Forman, W., & Jones, C., 1999, *ApJ*, 525, 47
- Voit, G. M., Bryan, G. L., Balogh, M. L., & Bower, R. G., 2002, *ApJ*, 576, 601
- Voit, G. M., & Bryan, G. L., 2001, *Nature*, 414, 425
- White, D. A., 2000, *MNRAS*, 312, 663
- White, S. D. M., Navarro, J. F., Evrard, A. E., & Frenk, C. S., 1993, *Nature*, 366, 429
- Wu, X.-P., 2000, *MNRAS*, 316, 299
- Wu, X.-P., Chiueh, T., Fang, L.-Z., & Xue, Y.-J., 1998, *MNRAS*, 301, 861
- Yaqoob, T., 1999, *ApJ*, 511, 75
- Zakamska, N. L., & Narayan, R., 2003, *ApJ*, 582, 162
- Zhang, Y.-Y., & Wu, X.-P., 2003, *ApJ*, 583, 529